



LAWRENCE
LIVERMORE
NATIONAL
LABORATORY

Relative contributions of mean changes and ENSO-driven variability to precipitation changes in a warming climate

C. Bonfils, B. Santer, T. Phillips, K. Marvel, R. Leung, C. Doutriaux, A. Capotondi

November 5, 2014

Journal of Climate

Disclaimer

This document was prepared as an account of work sponsored by an agency of the United States government. Neither the United States government nor Lawrence Livermore National Security, LLC, nor any of their employees makes any warranty, expressed or implied, or assumes any legal liability or responsibility for the accuracy, completeness, or usefulness of any information, apparatus, product, or process disclosed, or represents that its use would not infringe privately owned rights. Reference herein to any specific commercial product, process, or service by trade name, trademark, manufacturer, or otherwise does not necessarily constitute or imply its endorsement, recommendation, or favoring by the United States government or Lawrence Livermore National Security, LLC. The views and opinions of authors expressed herein do not necessarily state or reflect those of the United States government or Lawrence Livermore National Security, LLC, and shall not be used for advertising or product endorsement purposes.

Relative contributions of mean-state shifts and ENSO-driven variability to precipitation changes in a warming climate

Céline J.W. Bonfils^{1*}, Benjamin D. Santer¹, Thomas J. Phillips¹,

Kate Marvel^{1,2}, L. Ruby Leung³, Charles Doutriaux¹, Antonietta Capotondi⁴

¹ Program for Climate Model Diagnosis and Intercomparison (PCMDI), Lawrence Livermore National Laboratory, Livermore, CA 94550, USA

² now at NASA Goddard Institute for Space Studies and Columbia University Department of Applied Physics and Applied Mathematics, New York, NY

³ Pacific Northwest National Laboratory, Richland, WA 99352, USA

⁴ University of Colorado and NOAA Earth System Research Laboratory, Boulder, CO, USA

* bonfils2@llnl.gov.

LLNL-JRNL-663825

Submitted to *Journal of Climate*: 05/11/2015, revised: 09/28/2015

The El Niño-Southern Oscillation (ENSO) is an important driver of regional hydroclimate variability through far-reaching teleconnections. This study uses simulations performed with Coupled General Circulation Models (CGCMs) to investigate how regional precipitation in the 21st century may be affected by changes in both ENSO-driven precipitation variability and slowly-evolving mean rainfall. First, a dominant, time-invariant pattern of canonical ENSO variability (cENSO) is identified in observed SST data. Next, the fidelity with which 33 state-of-the-art CGCMs represent the spatial structure and temporal variability of this pattern (as well as its associated precipitation responses) is evaluated in

simulations of 20th century climate change. Possible changes in both the temporal variability of this pattern and its associated precipitation teleconnections are investigated in 21st century climate projections. Models with better representation of the observed structure of the cENSO pattern produce winter rainfall teleconnection patterns that are in better accord with 20th century observations and more stationary during the 21st century. Finally, the model-predicted 21st century rainfall response to cENSO is decomposed into the sum of three terms: 1) the 21st century change in the mean state of precipitation; 2) the historical precipitation response to the cENSO pattern; and 3) a future enhancement in the rainfall response to cENSO, which amplifies rainfall extremes. By examining the three terms jointly, this conceptual framework allows the identification of regions likely to experience future rainfall anomalies that are without precedent in the current climate.

1. Introduction

Droughts and floods have profound societal and economic impacts. It is therefore imperative to better understand the mechanisms affecting the mean state and variability of precipitation (P). In the simplest heuristic model, future changes in regional P result from a gradual change in mean seasonal P, which is superimposed upon P teleconnection patterns arising from largely unaltered internal climate variability modes (such as ENSO; Collins et al. 2010).

A number of physical mechanisms have been proposed as contributory factors to the change in mean P in a warmer climate. These include: 1) the “wet-get-wetter” mechanism (Held and Soden 2006) associated with an increase in tropospheric water vapor; 2) global energy balance constraints, which reduce the percentage increase in global-mean P arising from GHG-induced surface and tropospheric warming (relative to the percentage increase in water vapor caused by the same GHG-driven warming; Allen and Ingram 2002); 3) the poleward displacement of current zonal wet-dry patterns as a result of shifts in atmospheric circulation, which affect the horizontal and vertical transport of water vapor (Marvel and Bonfils 2013; Seidel et al. 2008); and 4) the “warmer-get-wetter” mechanism linking the patterns of tropical SST changes and rainfall changes (with tropical rainfall shifting to regions where the SST increase exceeds the tropical-mean warming; Xie et al. 2010).

Understanding the changes in P variability in a warmer climate is challenging for at least two reasons. First, while most climate models consistently project an increase in the frequency of extreme ENSO events under increased GHG forcing (Cai et al. 2014, 2015; Capotondi, 2015), there is considerable model disagreement in projected 21st century changes in the spatial structure and amplitude of ENSO (Coelho and Goddard 2009; Collins et al. 2010; Kao and Yu 2009; Vecchi and Wittenberg 2010). This yields substantial inter-model differences in projected future hydrological changes, both in the tropics and in

regions affected by ENSO-driven teleconnections (Meehl and Teng 2007; Kug et al. 2010; Stevenson 2012).

Second, there are also large uncertainties in how ENSO-mediated tropical and extratropical P responses are influenced by GHG-induced changes in the mean state, e.g., due to spatially non-uniform tropical SST warming, or changes in atmospheric circulation and moisture content (see Huang et al. 2013; Meehl and Teng 2007; Ruff et al. 2012; Seager et al. 2012; Stevenson et al. 2012). The latter issue is important, even if the spatial and temporal characteristics of ENSO are unaltered in the future climate. For example, Watanabe et al. (2014) show that ENSO-induced P variability will increase in the equatorial Pacific under global warming, even in the absence of a robust change in SST variability.

A number of recent studies have relied on single-model AGCM simulations forced with idealized patterns of greenhouse warming and El Niño-induced SST changes. To study the origin of the projected 21st century intensification of El-Niño-driven precipitation variability in the central and eastern equatorial Pacific, Power et al. (2013) performed a set of idealized AGCM simulations. They found that the contribution of 21st century changes to the amplitude of ENSO-driven SST variability is secondary compared with nonlinear ENSO responses to mean surface ocean warming. In a complementary study, Chung et al. (2014) showed that the projected tropical Pacific P response to El Niño events strongly depends on the spatial structure of the imposed warming.

Further insights were provided by Zhou et al. (2014), who generated three ensembles of idealized AGCM simulations forced with a 2-year-long El Niño composite of SST anomalies (see their Figure 2). Two of these sets of simulations also included an SST warming field which was either spatially uniform or displayed a prescribed pattern. Although the El Niño composite incorporated the full development and decay of an ENSO event, the authors only analyzed the results for the December-February (DJF) season. They found that in both the uniform and non-uniform warming cases, the imposed SST warming substantially reduced the barrier to deep convection in the eastern equatorial Pacific, causing the El Niño-induced P response in DJF to intensify and move eastward. In turn, the shifted anomalies in tropical convection forced the Pacific–North American (PNA) teleconnection pattern to move eastward and intensify. All changes were larger when a non-uniform pattern of SST warming was prescribed. Zhou et al. (2014) confirmed these results using Atmospheric Modeling Intercomparison Project (AMIP) simulations forced by: 1) the time-varying observed SST evolution over 1979–2008 (instead of a 2-year idealized El Niño composite); 2) a superimposed spatially uniform SST increase (“amip4K” experiments), or 3) a superimposed global spatially patterned SST increase (“amipFuture” experiments).

In the present study, we use simulation output from fully coupled atmosphere-ocean GCMs to partition future P anomalies into changes in the mean state of P, ENSO-driven P variability, and a future enhancement in the P response to ENSO.

We investigate the near-global pattern of P responses to both phases of ENSO using 71 simulations of historical and future climate change from Phase 5 of the Coupled Model Intercomparison Project (CMIP5; Taylor et al. 2012). The 21st century climate change results are for the Representative Concentration Pathway 8.5. This choice is justifiable because the current carbon dioxide emissions continue to track slightly above this high-end emission pathway (Peters et al. 2013). Splicing the historical simulations (which typically end in December 2005) with the RCP8.5 runs facilitates the comparison with observations over a longer period of the observational record. The spliced CGCM simulations, referred to subsequently as HIST+8.5, encapsulate our best quantitative estimates of future changes in the mean climate state, in the ENSO mode of variability, and in their respective uncertainties (arising from differences in model structure, forcing, and responses).

While use of a large multi-model ensemble is advantageous for identifying robust teleconnection behavior, the diagnosis of results from coupled simulations also presents certain challenges. First, because SSTs in CMIP5 models are predicted instead of prescribed, teleconnection properties are sensitive to inter-model differences in both the mean-state changes and in the amplitude and structure of ENSO-driven SST variability (Coats et al. 2013; Meehl and Teng 2007; Stevenson 2012). Second, certain features of the P response to global warming resemble ENSO-induced P variability (Lu et al. 2008; Marvel and Bonfils 2013), thus complicating the interpretation of simulated P changes. Third, coupled model

errors in ENSO characteristics (Capotondi et al. 2015a; Guilyardi et al. 2009) and in the P mean state (Marvel and Bonfils 2013) impact the simulation of ENSO-driven P responses (Coelho and Goddard 2009; Joseph and Nigam 2006; Langenbrunner and Neelin 2013).

Our analysis strategy relies on the identification of a dominant, time-invariant pattern of canonical ENSO (cENSO)¹ SST variability in observations. We are aware that ENSO exhibits a diverse range of spatial patterns, with SST anomalies peaking at different longitudes, as described in an extensive recent literature that is summarized in Capotondi et al. (2015b). However, given the large inter-model spread in present-day ENSO simulations, as well as the large uncertainty in projected ENSO changes, we find it useful to focus on one “typical” ENSO pattern. This pattern is then used to study the stationarity and amplitude of P teleconnections, their contribution to future changes in P, and the impact of model quality on the 21st century projections.

Analyzing the underlying thermodynamic and dynamical mechanisms associated with the ENSO-driven P change under global warming is outside of the scope of this study. Instead, based on our single, time-invariant cENSO pattern, we develop a simple common framework useful for determining: 1) how well different models capture a key mode of observed internal variability; 2) how the amplitude of this

¹ Here the term “canonical” is used to describe “standard”, or “typical” ENSO events; it does not imply that the cENSO mode is derived from canonical correlation analysis.

mode evolves in observations and coupled models²; and 3) whether a better simulation of the observed cENSO pattern translates to improved performance in simulating observed teleconnection behavior. This framework is also useful for decomposing the model-predicted changes in P into different components.

2. Datasets and Methods

a. Observed cENSO mode

We estimate the cENSO mode by Empirical Orthogonal Function (EOF) analysis of two different observational datasets (section S1): version 3b of the NOAA Extended Reconstructed SST dataset (ERSSTv3b; (Smith et al. 2008) and version 1.1 of the UK Meteorological Office Hadley Centre Sea Ice and SST dataset (HadISST1.1; (Rayner et al. 2006). We first computed local (grid-point) monthly-mean SST anomalies (SSTA) relative to the climatological annual cycle over 1900 to 1909. The choice of the reference period is primarily for visualization purposes, and does not affect the main findings of this study. In order to remove an overall global-scale warming signal and focus attention on internal variability, we subtracted the time-evolving global-mean SSTA (GMSSTA) from the local SSTA, yielding the monthly-mean SST residuals (SSTR). The SSTR and their EOFs have, by construction, an area-weighted spatial average of zero. The cENSO mode (Fig. 1a) is then defined as the leading EOF of the monthly-mean SSTR covariance matrix (see section S4 for further details). The cENSO pattern resembles previously described drought-conducive SST anomaly patterns (Capotondi and

²In the idealized experiments, this amplitude is constant, or specified in advance.

Alexander 2010; Schubert et al. 2009). The associated cENSO principal component time series (cENSO-PC1, Fig. 1b) is highly correlated with the observed Niño3.4 index (not shown) with a correlation of $r_{1902-2012}=0.85$. Performing the EOF analysis using SSTR (instead of using SSTA) better separates the leading mode of ENSO variability from a global-scale warming signal. This signal is evident in the second EOF of SSTR (Fig. 1d-e; see also section S5 and Fig. S1).

b. El Niño life cycle estimated from the observed cENSO mode

Although cENSO is a single, time-invariant mode, it can successfully reproduce important aspects of the ENSO life cycle. To illustrate this, the life cycle of El Niño is calculated as the 24-month composite of the cENSO-PC1 time-series for 5 major El Niño events (1972/73, 1982/83, 1987/88, 1997/98 and 2009/2010; event selection follows Zhou et al., 2014). The composite time series are computed from January of the year of El Niño development (year 0) to December of the year of its decay (year+1). To allow a direct comparison with Figure 2 of Zhou et al. (2014), which shows the observed time-longitude SST evolution of a typical El Niño event, we projected our 24-month composite onto the spatial average (over 5°N to 5°S) of the cENSO pattern at discrete longitudes (in the range 120°E-80°W; see Fig. 1c). By definition, our time-invariant cENSO mode cannot capture the eastward propagation of positive SST anomalies seen in Figure 2 of Zhou et al. (2014). We note, however, that other aspects of the Zhou et al. ENSO life cycle are well-replicated: warm anomalies develop in the central Pacific in summer, peak in winter of year 0, and then decay, followed by a La Niña event in year 1 (Fig. 1c).

c. Observed cENSO-driven hydrological responses

We use three different hydrological variables to illustrate the influence of the cENSO mode on regional hydroclimate: 1) column-integrated water vapor over oceans (W), measured by the satellite-based Special Sensor Microwave Imager (SSM/I; Mears et al. 2007); 2) precipitation (P) estimated from the Global Precipitation Climatology Project (GPCP) data (Adler et al. 2003); and 3) the continental Palmer Drought Severity Index, calculated using the Penman-Monteith potential evapotranspiration (PDSI; Dai 2011; Dai et al. 2004). For each variable, anomalies were defined relative to the climatological annual cycle computed over the full observational period of the data set. We then performed an EOF analysis and identified the leading observed W, P, and PDSI PC time series (see Fig. 2a) that are most highly correlated with the observed cENSO-PC1 (PC1 for W and P, and PC2 for PDSI, consistent with Dai et al., 2004).

To estimate the cENSO-driven hydrological teleconnection patterns, we calculated r_{DJF} , the contemporaneous correlation between the seasonal-mean (DJF only) time series of cENSO-PC1 and the local W, P, or PDSI (Fig. 2b-d). Additionally, we computed $r\{k\}$, which relies on monthly-mean time series for all calendar months (Fig. S2a-c). The lag k is the value of k (in months) that maximizes r at each location. Teleconnections calculated using r_{DJF} and $r\{k\}$ yield very similar results; the latter are primarily influenced by the strong teleconnections in DJF.

d. HIST+8.5 simulations

After regridding to a common T42 horizontal grid (see section S3), we analyze model SST and P data from: 1) CMIP5 HIST simulations with estimated historical changes in anthropogenic and natural forcings; and 2) RCP8.5 simulations forced by projected 21st century changes in GHGs and anthropogenic aerosols. Model SSTRs were defined as for the observations, with subtraction of each model's local climatological monthly-mean and global-mean SSTA.

For each model, SSTRs were used for two purposes: calculating the model cENSO mode, and projecting onto the observed cENSO mode (Bonfils and Santer 2011). The model cENSO mode calculation allows direct comparison with the observational cENSO pattern (see section S4). The projection of each model's SSTRs onto the observed cENSO pattern yields “pseudo-principal component” time series (not shown), which capture the temporal evolution of the spatial covariance between the observed cENSO pattern and the time-varying model SSTRs. Pseudo-PCs were employed to: 1) assess how well models reproduce the observed magnitude of global-scale SST variability associated with cENSO³; and 2)

³ Pseudo PCs are often used in pattern-based detection and attribution studies, in which a model-predicted anthropogenic fingerprint is searched for in observations (see, e.g. Santer et al. 2009). They also have been used to investigate the aliasing of a large-scale anthropogenic warming signal in the Pacific Decadal Oscillation index (Bonfils and Santer, 2011) and to assess model quality in simulating the Madden-Julian Oscillation (Sperber and Kim 2012). Sperber et al. (2005) have noted that use of different basis functions (e.g., leading EOFs estimated separately from observations and individual models) can hamper interpretation of inter-model and model-versus-observational differences. In contrast, projecting observational and model data onto a common basis function – as we do here – facilitates the direct

calculate the model cENSO-driven P teleconnection patterns over the 20th and 21st centuries (Fig. 2e-f; Fig. S2d-e; Fig S4). As in the case of the observations, the model P teleconnection pattern is the contemporaneous correlation (or the maximum absolute value of the lagged correlation) between each model's pseudo-PC and its local P time series.

e. Model performance metrics

We used three performance metrics to assess each model's ability to replicate the observed cENSO mode. These metrics gauge the fidelity with which the models represent the spatial structure of the observed cENSO pattern (r_{EOF1} ; Fig. 3a and S5a), the amplitude of the observed temporal variability of cENSO-PC1 (σ ; Fig. 3a and S5b), and the observed pattern of teleconnections between the variability of cENSO and precipitation (r_{TEL} ; Fig. 3b and S5c-d). The r_{EOF1} metric is the centered spatial correlation between the observed cENSO pattern (Fig. 1a) and each simulated cENSO pattern (see Fig. S3). The $\sigma_{1979-2012}$ metric is the temporal standard deviation of the monthly-mean pseudo-PCs, calculated over the 34-year period of satellite-based SST measurements. Finally, the metric r_{TEL} is the centered⁴ spatial correlation between the simulated and observed precipitation teleconnection patterns (Fig. S4). Further details of these metrics are given in section S6 of the Supplemental Material.

comparison of modeled and observed teleconnection behavior. We are not aware of any other paper in the literature that uses pseudo-PC time series to calculate P teleconnections.

⁴ The centered statistic measures the similarity of two patterns after removal of their spatial means.

f. Composite analyses

The P teleconnection patterns are estimated by correlating each model's pseudo-PC and its local P time series. Correlations are bounded between -1 and 1, and are insensitive to differences in the amplitude of the two time series being correlated⁵. We therefore decided to use a composite analysis of ENSO events (as in Stevenson 2012 and Meehl and Teng 2007) to investigate changes in the amplitude of the P response to ENSO events. Two types of composite analyses (CA) were performed in this study. For each CA and each simulation, large La Niña-like and El Niño-like events were identified from the detrended model pseudo-PC time series, using an amplitude threshold of >1 or <-1 , respectively. We then averaged the corresponding DJF P response for each set of events. The P anomaly time series were not detrended in CA #1, but were in CA #2. Over the 1900-1999 period, the two composites yield very similar results, because P time series show relatively small trends over this period. Over the 2000-2099 period, however, CA #1 (Fig. 4a) captures both the change in P mean state (Fig. 4c) and any change in the ENSO-induced variability of P (Fig. 4b). In contrast, CA #2 largely reflects the cENSO-driven P variability. By comparing the results of CA #2 for the 1900-1999 and the 2000-2099 periods, we can identify a change in cENSO-driven P variability between the two centuries (Fig. 4d). Seager et al. (2012) used a similar technique to determine whether global warming causes intensified interannual variability in P-E.

⁵ In consequence, amplification of the P response to ENSO events in the 21st century does not necessarily yield larger absolute values of the correlation coefficients.

3. Results

a. Observed teleconnections

To account for the pronounced seasonality of ENSO teleconnections, and to compare our results with those of idealized AGCM experiments, our analysis (unless otherwise indicated) focuses on DJF, the peak season of ENSO impact. Figure 2a shows that the cENSO-PC is highly correlated with the leading PC of column-integrated water vapor over oceans ($r_{[1988-2008]}=0.85$) and PC1 of precipitation ($r_{[1979-2012]}=0.82$), as well as with the second PC of the continental PDSI ($r_{[1902-2008]}=0.82$). In terms of the spatial patterns of these relationships, we find that extensive areas of the tropics are characterized by strong negative and positive correlations between cENSO variability and changes in hydroclimate (Figs. 2b-d). Despite differences in measurement platforms, instrumentation, spatial coverage, and the length of the observational record, the teleconnection patterns in the P, W, and PDSI fields are very similar (Figs. 2b-d). This clearly illustrates that the temporal behavior of the cENSO pattern has a broad influence on a variety of interrelated aspects of hydroclimatic variability (Dai and Wigley 2000; Dai et al. 2004; Trenberth et al. 2005).

In the positive phase of the cENSO pattern (corresponding here to a La Niña event), the colder central-eastern equatorial Pacific is associated with reduced precipitation, while enhanced precipitation occurs in the far western Pacific and

over the Maritime Continent (Fig. 2c). Over land, drier conditions prevail across southern North America, east Africa, and southern South America, while wetter conditions are found in northern South America, south Africa, south-west India, and some parts of Australia, in agreement with results from previous studies (e.g., Dai and Wigley, 2000).

b. Model performance evaluation

We first employ the r_{EOF1} metric to identify the models with the best representation of the observed cENSO pattern. The r_{EOF1} values span the range 0.62 to 0.91; the associated model rankings are given in Fig. S5a. We use the ranked r_{EOF1} results (Fig. S5a) to select the “TOP20” models ($r_{\text{EOF1}} > 0.83^6$). Since model errors are complex functions of space, time, and variable (see, e.g., Santer et al. 2009), alternate metric choices would likely yield different model rankings. For our specific application, however, model performance in representing the observed cENSO pattern is of primary importance for accurate simulation of cENSO-driven teleconnection patterns. This provides considerable justification for our use of r_{EOF1} to select better performing models.

The TOP20 models are markedly more successful in reproducing both the observed amplitude of cENSO temporal variability ($\sigma_{1979-2012}$, Fig. 3a) and the cENSO-driven P teleconnection patterns (r_{TEL}), irrespective of whether these

⁶ The choice of 20 models is motivated by Fig. S5a, which naturally separates the models into two groups: those with $r_{\text{EOF1}} > 0.83$, and with relatively small inter-model correlation differences, and those with much lower r_{EOF1} values. We did not use other criteria to select the “best” models.

metrics are calculated using all months (Figs. 3b) or all DJFs of the pseudo-PCs (Fig. S5e). For example, in both the “all months” and “individual DJF” cases, 17 of the models that best capture the observed r_{TEL} pattern are in the TOP20 set. Similarly, most models that produce a pseudo-PC time series with temporal variability that is smaller than observed are also unable to satisfy the TOP20 r_{EOF1} -based criterion (Fig. 3a)⁷.

c. Changes in cENSO

Models that perform well in reproducing the spatial structure of the observed cENSO pattern (r_{EOF1}) also tend to display larger amplitude of cENSO and Niño3.4 variability for the historical period. We note, however, that the r_{EOF1} metric does not help to reduce the spread of model results in the change in amplitude of the 21st century temporal variability of the cENSO pattern (Fig. 3c). The TOP20 models (all denoted by solid symbols) do not project a robust increase or reduction in cENSO variability. A comparison of the 20th and 21st century results indicates that 5 TOP20 models project an increase in magnitude of the cENSO variability (cesm1_cam5, cmcc_cms, gfdl_cm3, mpi_esm_lr, mpi_esm_mr), 5 models project a reduction in cENSO variability (ccsm4, gfdl_esm2m, hadgem2_es, ipsl_cm5a_mr, noresm1-m), and 10 models display no appreciable change

⁷ Relatively low temporal variance in the pseudo-PC may occur because of two factors: 1) the observed tropical Pacific variability is underestimated in the model of interest; and/or 2) the simulated amplitude of tropical Pacific variability is realistic, but there are substantial spatial biases in the model SST fields, which result in poor projection of the simulated SST fields onto the observed cENSO pattern. The strong correlation across realizations between the amplitude of the variability of pseudo-PCs and Niño 3.4 time series (Fig. S5f) suggests that the simulated tropical Pacific SST variability is the main driver of the temporal variance in the pseudo-PCs. This supports hypothesis 1) above.

(access1_0, access1_3, bnu_esm, canesm2, cesm1_bgc, cmcc_cm, cnrm_cm5, hadgem2_ao, hadgem2_cc, noresm1-me). Most models that are not included the TOP20 group underestimate the observed temporal variability of the cENSO PC in the 20th century, and continue to project low pseudo-PC variability in the 21st century (Fig. 3c).

The observed cENSO pattern and all simulated SSTRs have an area-weighted spatial average of zero (see Section 2a). By definition, therefore, trends in the cENSO pseudo-PCs are insensitive to spatially uniform ocean warming, but should be sensitive to warming with a spatial structure resembling the cENSO SST pattern itself (section S5). Trends in the cENSO pseudo-PCs over 2000-2099 do not show consistent behavior across the CMIP-5 models (Fig. 3d). This appears to contradict results from several previous studies, which found that most CMIP5 models tend to produce more El Niño-like conditions in the 21st century (Bayr et al. 2014), with faster warming in the tropical eastern Pacific relative to the entire tropical Pacific basin (Power et al. 2013; Zhou et al. 2014). We hypothesize that this apparent contradiction arises from the effects of inter-model differences in extratropical SST variability (which are projected onto the cENSO pattern), rather than from the lack of a consistent El Niño-like mean SST warming pattern in response to increasing GHGs.

d. Spatial stationarity of ENSO-driven P patterns

For the TOP20 case, the multi-model average ENSO-driven P teleconnection pattern reproduces many key features of the observed pattern (Figs. 2c,e; Fig. S2b,d). This holds for calculations involving DJF only and all calendar months. The multi-model average P pattern in the TOP20 models (Fig. 2e) has smaller amplitude features than the corresponding observed pattern (Fig. 2c). This is mainly due to such factors as spatial smoothing (arising from averaging of results over realizations and models) and to inter-model differences in the spatial features of the teleconnection patterns, rather than to a muted P response in each individual model (Fig. S4). The simulated teleconnection patterns for the 20th and 21st centuries (which are both calculated relative to the 20th and 21st century mean states, respectively) are almost identical in the “all calendar months” calculations (Figs. S2e). This result implies that the cENSO-driven P teleconnection spatial patterns estimated from the TOP20 multi-model ensemble are largely stationary.

Over the DJF season (when ENSO-mediated P variability is most pronounced), the multi-model average P teleconnection patterns are very similar in the 20th and 21st centuries (Figs. 2e-f, $r_{1900-1999/2000-2099}=0.95$). When analyzed individually, however, the models (Fig. S4) show a large spread in the spatial similarity between their 20th and 21st century teleconnection patterns.

The spatial stationarity of DJF patterns is most pronounced in models with a large amplitude of DJF pseudo-PC variability in the 20th century (Fig. 3e). In contrast, models which underestimate temporal variability of the observed cENSO pattern

yield spatial DJF teleconnection patterns that are less stationary and more easily disrupted by other sources of internal variability (Coats et al. 2013). This suggests that the spatial stationarity metric is sensitive to the amplitude of cENSO events, which affects the degree to which deep convection is triggered in the tropical Pacific region (not shown), and thus the strength of the atmospheric teleconnections.

e. Amplification of the cENSO-driven P responses

In this section, we examine the individual components that contribute to the projected changes in 21st century P anomalies in response to ENSO variability (see Fig. 4 and Fig. S6). We first apply Composite Analysis #1 (section 2e), identifying all large La Niña-like and El Niño-like events from the model pseudo-PCs, and then averaging the corresponding total (i.e., non-detrended) DJF P response for each set of events. Over the 1900-1999 period, this analysis shows that the TOP20 models reliably capture many of the features of the observed pattern of P response to cENSO variability (Fig. 4b). When Composite Analysis #1 is performed over the 2000-2099 period (Fig. 4a), these features of the 20th century teleconnection pattern are still visible, but they are also imprinted with the change in the mean DJF P between the 20th and 21st centuries (Fig. 4c). This change in mean state is spatially complex. It is influenced by further moistening of the currently wet areas of the tropics and storm track regions, and by further drying of currently dry portions of the subtropics. This behavior is typically associated with the “wet-get-wetter” mechanism; (Held and Soden 2006; Huang et al. 2013). The pattern of

mean state change also reflects increased rainfall over the Equator relative to the southeast tropical Pacific, which is consistent with the “warmer-get-wetter” mechanism (Huang et al. 2013)⁸.

Assuming a linear response of P to the future behavior of ENSO, the total P associated with future ENSO events (Fig. 4a) should be well-described by summing the historical P responses to cENSO variability (Fig. 4b) and the change in mean P (Fig. 4c). However, a number of AGCM-based studies (e.g., Chung et al. 2014; Huang et al. 2013; Power et al. 2013; Zhou et al. 2014) suggest that such a simple partitioning of the P response provides an inadequate explanation for the projected changes in P . Since deep convection responds to SST thresholds, changes in equatorial SSTs due to global warming are expected to alter the atmospheric response to ENSO, even in absence of significant changes in 21st century ENSO events. To estimate this non-linear contribution to the total P response in the CGCMs, we followed the approach of Seager et al. (2012), and detrended both the model pseudo-PCs of SST and the model P data prior to constructing composites (CA #2). In most regions, the difference maps between the 20th and 21st century composites reveal an amplified P response to both El Niño and La Niña phases (Fig. 4d). In the El Niño case, the intensification is more pronounced in the central-eastern Pacific.

⁸ One caveat is that some component of the mean change in P could also be a result of ENSO-driven changes in the variability of P . Examples of such behavior might involve a change in the relative frequency of El Niño and La Niña events, or enhancement of the precipitation response to El Niño events (relative to La Niña events).

Is the amplified response solely caused by a projected change in the amplitude of ENSO-driven SST variability? To address this question, we estimated the nonlinear “missing term” using the three sets of models—those showing either an increase (σ_{\uparrow}), a decrease (σ_{\downarrow}) or no discernible projected change (σ_{\rightarrow}) in the amplitude of pseudo-PC variability between the 20th and 21st centuries. The results are displayed in Fig. 5. We find that the P variability is projected to intensify, even in absence of a change in cENSO amplitude (the σ_{\rightarrow} case). The amplification of P variability, however, is also modulated by the projected change in the magnitude of σ : it is larger in simulations where σ is projected to increase (σ_{\uparrow}), and damped in simulations where σ is projected to decrease (σ_{\downarrow}).

When near-future (2017-2050) and more distant future (2059-2092) 33-year⁹ periods are compared (Figs. S7-S8), it is evident that both the magnitude of the mean P change (panels c) and the amplification components (panels d and Fig. 5) become larger as the tropical mean SST warming increases and the GHG-forced global atmosphere becomes warmer and moister.

Consistent with previous findings, the TOP20 models show that the center of action of wintertime cENSO-driven P responses is projected to shift eastward in the equatorial Pacific and near the North American Pacific west coast (compare,

⁹ The 33-year analysis timescale is determined by the length of the GPCP observational dataset (which spans the period from 1979 to 2012). The two selected analysis periods are 38 years and 80 years after the beginning of the observational period.

for example, Figs. 4b and 4d for the El Niño case). To better understand this result, we compute, after Power et al. (2013), the P anomalies along the Equator for the El Niño case. Comparison of the solid and dashed black lines in Fig. 6a reveals that the amplification component in the eastern tropical Pacific is accompanied by a clear eastward shift of the positive P anomalies. This shift, which occurs even in the σ_{\rightarrow} simulations (blue lines) is accentuated in the σ_{\uparrow} simulations (red lines), but is reduced in the σ_{\downarrow} simulations (green lines). During La Niña events, the negative P anomalies intensify in the central Pacific in all cases (σ_{\rightarrow} , σ_{\uparrow} , σ_{\downarrow}). The 21st century negative P anomalies in the eastern tropical Pacific (east of 160°E) are also located eastward of their historical counterparts, especially in the σ_{\uparrow} simulations (red lines), as compared with the σ_{\downarrow} simulations (green lines). Given that the eastern equatorial Pacific is typically dry, except during El Niño events, the changes depicted in (b) are likely related to changes in the climatology, which in turn are related to the changes during El Niño events (see Fig. 6a, which shows little change in the green lines, and the greatest change between the red lines). Similar results from the North Pacific region are discussed in the next section.

4. Discussion

a. Mechanisms

As noted in the previous section, future DJF precipitation responses to ENSO-like events can be decomposed into the sum of three components: 1) a mean-state change in P; 2) the historical P anomalies in response to cENSO variability; and 3) a component capturing the future amplification and locational shift of the

historical P anomalies associated with ENSO (Figs. 4). Although component (3) is affected by model uncertainties in σ (the amplitude of the 21st century variability in the cENSO pseudo-PCs), this component amplifies the cENSO-driven P variability in most regions (Fig. S9), and increases the magnitude of cENSO-driven extreme dry/wet anomalies at locations already sensitive to ENSO events.

Several different mechanisms can be invoked to explain why the P responses to El Niño and La Niña are projected to intensify and shift eastward in the future. First, the Held and Soden (2006) “wet-gets-wetter” mechanism in a warmer and moister atmosphere does not operate exclusively on climatologically wet and dry features. This mechanism can also impact regions that are affected by ENSO and are experiencing either anomalously wet or dry conditions. The net effect is to further enhance wetting or drying of these regions, depending on the ENSO phase. Second, the mean SST warming and the detailed spatial pattern of the projected warming in the tropical Pacific (e.g., Chung et al. 2014; Zhou et al. 2014) both seem to play a major role in triggering the eastward shift and intensification of: 1) the main convection centers in the tropics (Fig. 6a-b); and 2) the teleconnected P responses in the North American sector (Fig. 6c-d).

Climatologically, the eastern Pacific is dry and cool, whereas the easterly trade winds drive warm water toward the western Pacific and create favorable conditions for upwelling of cold water in the east Pacific. The 21st century anthropogenic warming signal in most CMIP5 models tends to be larger in the

eastern equatorial Pacific than in the surrounding ocean waters (according to Bayr et al. 2014; Cai et al. 2014; Power et al. 2013). This asymmetric pattern of temperature change has been identified in coupled climate simulations (Vecchi et al. 2006), and is consistent with the weakening of the Walker circulation and surface easterly winds under global warming. The resulting reduction of the zonal SST gradients along the Equator weakens the barrier preventing eastern Pacific SST from triggering deep convection. In these conditions, even a small increase in SST can significantly alter atmospheric convection and favor a shift and intensification of P in the tropical eastern Pacific during warm events. Thus, if ENSO amplitude does not increase with global warming, the superposition of warm El Niño SST anomalies and the warmer background conditions can lead to an eastward displacement of convection and an increased frequency of extreme El Niño events (Cai et al. 2014; Chung et al. 2014; Kug et al. 2010; Power et al. 2013; Zhou et al. 2014).

Extreme La Niña events are also projected to become more frequent, as explained in Cai et al. (2015) and Capotondi (2015). During normal La Niña events, trade winds intensify and cause the central Pacific to become colder and drier, resulting in a westward shift of deep convection. These features are enhanced during extreme La Niña events, and deep convection shifts further west toward the Maritime Continent. Anthropogenic warming is projected to increase faster over the land masses in the Maritime Continent than in the central equatorial Pacific, resulting in an enhanced SST gradient between these two regions. As a

consequence, the anomalous trade winds become stronger in the area where the SST gradient increases, displacing water westward and poleward, and leading to enhanced upwelling. Due to the increased vertical temperature gradient (with surface waters warming faster than deeper water) the latter process will produce relatively colder anomalies in the central Pacific, and will further increase the temperature gradient between Maritime Continent and the central Pacific, favoring the development of extreme cold events. In the 21st century simulations, the enhanced reduction of precipitation in the central-eastern Pacific during La Niña events (Fig. 6b) is consistent with the projected increase in the frequency of extreme La Niñas.

In the mid- and high-latitudes, the climate responses to ENSO events strongly depend on the locations of tropical atmospheric convection centers, which affect the propagation pathways of atmospheric waves. In comparing idealized control and 2×CO₂ simulations from eight CMIP3 models, Kug et al. (2010) show that: 1) tropical Pacific SST increases resulting from GHG warming promote the eastward shift of the main tropical convections centers associated with both El Niño and La Niña (in accord with our results); and 2) the eastward shift of tropical convection anomalies results in systematic eastward shifts in the mid-latitude DJF precipitation teleconnection pattern, again during both ENSO phases. In the North American sector we find a similar eastward shift of P anomalies in response to both El Niño and La Niña in the σ_{\rightarrow} and σ_{\downarrow} cases (Fig. 6c-d). In the σ_{\uparrow} case, the increase (decrease) in P anomalies in response to El Niño (La Niña) occurs at all

longitudes. The analysis of Zhou et al. (2014), which is most comparable to the to our σ_{\rightarrow} / El Niño case, yields analogous results, with the spatial pattern of tropical SST warming producing larger teleconnections changes than a spatially uniform warming.

b. Three-term decomposition

With few exceptions (Watanabe et al. 2014; Wittenberg 2015), most previous studies focus on individual components of projected P changes: either the change in mean P, the historical P variability, or the change in P variability (i.e., the non-linear term). Here, we consider the combined effects of these three components on regional scales. Because changes in mean and variability are both spatially complex, it is difficult to intuitively predict how the total P anomalies will behave in a particular region (relative to some historical reference).

Our simple three-term decomposition framework provides a quantitative estimate of the relative importance of each of these terms in different geographical regions (Fig. 7). It also helps to identify regions where the projected 21st century P responses to cENSO variability are without precedent in the current climate. For example, an amplified P response to both cENSO phases is projected over the northeastern Pacific region. Here, however, the future P response to La Niña lies within the range of historical variability, while the future response to El Niño is projected to be outside of the range of historical P responses. In the southwestern United States, the dry conditions in response to future La Niña events are

projected to be outside of the range of historical P responses. In contrast, the change in mean P over Mexico always yields drier than historical conditions, independent of the cENSO phase. These three examples illustrate that reliable assessment of flood- and drought-risk in the future must rely on estimates of all three components discussed here.

5. Conclusions

Future ENSO-driven P responses are sensitive to changes in both the mean state of P and to changes in the amplitude and structure of ENSO-driven P variability. To investigate how ENSO-driven P variability may change in a warming climate, many previous studies have relied on single-model AGCM simulations forced with idealized greenhouse warming patterns, and/or with an idealized El Niño-induced SST pattern (with pre-determined amplitudes) superimposed on some pre-determined global-mean SST change. In this study, we rely instead on CGCM multi-model HIST+8.5 simulations. Here, we seek to: 1) identify a time-invariant canonical ENSO (cENSO) pattern in observed SST data; 2) project the simulated SSTs onto the observed cENSO mode; 3) sort the simulations according to whether they produce an increase, a decrease, or no significant change in the magnitude of the cENSO variability in the 21st century; 4) calculate various measures of model performance in capturing observed cENSO characteristics, and observed teleconnection relationships between temporal variability in the cENSO pattern and local P; and 5) develop a simple heuristic model to partition 21st century P changes into mean state and variability components.

We find that CGCMs with better representation of the structure and variability of the observed cENSO produce rainfall teleconnection patterns that are in better accord with observations. We hypothesize that simulations with larger amplitude cENSO variability trigger deeper convection in the tropical Pacific region, thereby forcing atmospheric teleconnection patterns that remain more stationary through time (Section 3d). Finally, we find that most regions of the globe exhibit enhanced anomalies in future P as a response to both El Niño- and La Niña-like phases. This change in P is accompanied by a clear eastward shift of teleconnection patterns in the Equatorial Pacific and in the North Pacific, which occurs even in the absence of a robust increase in cENSO variability amplitude.

Our study investigates the effects of a time-invariant, observationally-derived ENSO pattern on the geographical pattern of P anomalies. This relationship is explored in the context of both 20th and 21st century climate change. Although our focus is specifically on this canonical ENSO mode, it is clearly possible that other natural modes of SST variability might alter existing teleconnections between SST and P. It is beyond the scope of this paper to consider how ENSO-driven P responses might be affected by: 1) a change in the SST structure of ENSO, including the recent prevalence of central-Pacific over east-Pacific El Niño events (Yeh et al. 2009); 2) GHG-induced changes in other modes of variability; and 3) a seasonal shift in the ENSO life cycle. Such issues merit further investigation.

As discussed in section 4, the amplification of the ENSO precipitation response in the eastern Pacific and the corresponding eastward shift of the precipitation pattern may be associated with a projected enhanced warming trend in the eastern equatorial Pacific. This pattern of warming may result from a weakening of the Walker circulation seen in some models (Vecchi et al. 2006) and in observations (Tokinaga et al. 2012). However, this view has been challenged by other observational studies (L'Heureux et al. 2013; Sandeep et al. 2014) which suggest that the Walker circulation may instead have strengthened over the past century. This strengthening is consistent with a cooling trend found in the eastern Pacific in several observational SST datasets after statistical removal of the ENSO mode (Compo and Sardeshmukh 2010; Karlauskas et al. 2009; Solomon and Newman 2012)¹⁰. There remain, therefore, important uncertainties in the projected changes in SST and precipitation, as well as in their causes. Reducing uncertainties in projections of 21st century ENSO behavior and related teleconnections may require several decades of research. Despite these significant uncertainties, our study establishes a useful conceptual framework for decomposing and analyzing projected changes in regional precipitation. This framework may help to inform important current and future decisions regarding food security and water resource management.

¹⁰ Likewise, Fig. 1b shows a positive trend in the cENSO-PC₁ time-series over the instrumental interval, which is consistent with a recent shift towards more La Niña-like conditions.

Acknowledgments

We acknowledge the World Climate Research Programme's Working Group on Coupled Modelling, which is responsible for CMIP, and we thank the climate modeling groups (listed in Table S1 of this paper) for producing and making available their model output. For CMIP the U.S. Department of Energy's Program for Climate Model Diagnosis and Intercomparison provides coordinating support and led development of software infrastructure in partnership with the Global Organization for Earth System Science Portals. CMIP5 data processing was enabled by the CDAT analysis package. A. Dai (University at Albany) calculated the second PC of the PDSI dataset (as in Figure 2d). This work was supported by the Climate and Environmental Sciences Division (CESD) and the Regional and Global Climate Modeling (RGCM) Program of the U.S. Department of Energy (DOE) Office of Science and was performed under the auspices of the U.S. DOE Lawrence Livermore National Laboratory (Contract DE-AC52-07NA27344). K.M. was supported by a Laboratory Directed Research and Development award (13-ERD-032). C.B. was fully supported by the DOE/OBER Early Career Research Program Award SCW1295. We would like to thank our three reviewers their very helpful and constructive comments, which we believe have improved the paper substantially.

References

- Adler, R., and Coauthors, 2003: The version-2 global precipitation climatology project (GPCP) monthly precipitation analysis (1979-present). *Journal of Hydrometeorology*, **4**, 1147-1167.
- Allen, M., and W. Ingram, 2002: Constraints on future changes in climate and the hydrologic cycle. *Nature*, **419**, 224-+.

- Bayr, T., D. Dommenges, T. Martin, and S. Power, 2014: The eastward shift of the Walker Circulation in response to global warming and its relationship to ENSO variability. *Climate Dynamics*, **43**, 2747–2763.
- Bonfils, C., and B.D. Santer, 2011: Investigating the possibility of a human component in various Pacific Decadal Oscillation indices. *Climate Dynamics*, **37**, 1457–1468.
- Cai, W., and Coauthors, 2014: Increasing frequency of extreme El Niño events due to greenhouse warming. *Nature Clim. Change*, **4**, 111–116.
- , 2015: Increased frequency of extreme La Niña events under greenhouse warming. *Nature Clim. Change*, **5**, 132–137.
- Capotondi, A., 2015: Atmospheric Science: Extreme La Niña events to increase. *Nature Clim. Change*, **5** (2), 100–101.
- Capotondi, A., and M. Alexander, 2010: Relationship between precipitation in the Great Plains of the United States and global SSTs: insights from the IPCC AR4 models. *Journal of Climate*, **23**, 2941–2958.
- Capotondi, A., Y.-G. Ham, A. Wittenberg, and J.-S. Kug, 2015a: Climate model biases and El Niño Southern Oscillation (ENSO) simulation. *U.S. Clivar Variations*, 21–25.
- Capotondi, A., and co-Authors, 2015b: Understanding ENSO Diversity. *Bull. Amer. Meteor. Soc.*, **96**, 921–938, doi: 10.1175/BAMS-D-13-00117.1
- Chung, C., S. Power, J. Arblaster, H. Rashid, and G. Roff, 2014: Nonlinear precipitation response to El Niño and global warming in the Indo-Pacific. *Climate Dynamics*, **42**, 1837–1856.
- Coats, S., J. E. Smerdon, B. I. Cook, and R. Seager, 2013: Stationarity of the tropical Pacific teleconnection to North America in CMIP5/PMIP3 model simulations. *Geophysical Research Letters*, **40**, 4927–4932.
- Coelho, C., and L. Goddard, 2009: El Niño-induced tropical droughts in climate change projections. *Journal of Climate*, **22**, 6456–6476.
- Collins, M., and Coauthors, 2010: The impact of global warming on the tropical Pacific ocean and El Niño. *Nature Geoscience*, **3**, 391–397.
- Compo, G., and P. Sardeshmukh, 2010: Removing ENSO-Related Variations from the Climate Record. *Journal of Climate*, **23**, 1957–1978.
- Dai, A., 2011: Characteristics and trends in various forms of the Palmer Drought Severity Index during 1900–2008. *Journal of Geophysical Research-Atmospheres*, **116**.
- Dai, A., and T. Wigley, 2000: Global patterns of ENSO-induced precipitation. *Geophysical Research Letters*, **27**, 1283–1286.
- Dai, A., K. Trenberth, and T. Qian, 2004: A global dataset of Palmer Drought Severity Index for 1870–2002: Relationship with soil moisture and effects of surface warming. *Journal of Hydrometeorology*, **5**, 1117–1130.
- Guilyardi, E., and Coauthors, 2009: Understanding El-Niño in ocean-atmosphere general circulation models - Progress and Challenges. *Bulletin of the American Meteorological Society*, **90**, 325–+.
- Held, I., and B. Soden, 2006: Robust responses of the hydrological cycle to global warming. *Journal of Climate*, **19**, 5686–5699.
- Huang, P., S. Xie, K. Hu, G. Huang, and R. Huang, 2013: Patterns of the seasonal response of tropical rainfall to global warming. *Nature Geoscience*, **6**, 357–361.
- Joseph, R., and S. Nigam, 2006: ENSO evolution and teleconnections in IPCC's twentieth-century climate simulations: Realistic representation? *Journal of Climate*, **19**, 4360–4377.
- Kao, H., and J. Yu, 2009: Contrasting eastern-Pacific and central-Pacific types of ENSO. *Journal of Climate*, **22**, 615–632.
- Karnauskas, K., R. Seager, A. Kaplan, Y. Kushnir, and M. Cane, 2009: Observed Strengthening of the Zonal Sea Surface Temperature Gradient across the Equatorial Pacific Ocean. *Journal of Climate*, **22**, 4316–4321.
- Kug, J., S. An, Y. Ham, and I. Kang, 2010: Changes in El Niño and La Niña teleconnections over North Pacific-America in the global warming simulations. *Theoretical and Applied Climatology*, **100**, 275–282.
- L'Heureux, M., S. Lee, and B. Lyon, 2013: Recent multidecadal strengthening of the Walker circulation across the tropical Pacific. *Nature Climate Change*, **3**, 571–576.
- Langenbrunner, B., and J. Neelin, 2013: Analyzing ENSO teleconnections in CMIP models as a measure of model fidelity in simulating precipitation. *Journal of Climate*, **26**, 4431–4446.
- Lu, J., G. Chen, and D. Frierson, 2008: Response of the zonal mean atmospheric circulation to El Niño versus global warming. *Journal of Climate*, **21**, 5835–5851.
- Marvel, K., and C. Bonfils, 2013: Identifying external influences on global precipitation. *Proceedings of the National Academy of Sciences*, **110**, 19301–19306.
- Mears, C., B. Santer, F. Wentz, K. Taylor, and M. Wehner, 2007: Relationship between temperature and precipitable water changes over tropical oceans. *Geophysical Research Letters*, **34**.

- Meehl, G., and H. Teng, 2007: Multi-model changes in El Nino teleconnections over North America in a future warmer climate. *Climate Dynamics*, **29**, 779-790.
- Peters, G., and Coauthors, 2013: Commentary: The challenge to keep global warming below 2 degrees C. *Nature Climate Change*, **3**, 4-6.
- Power, S., F. Delage, C. Chung, G. Kociuba, and K. Keay, 2013: Robust twenty-first-century projections of El Nino and related precipitation variability. *Nature*, **502**, 541-+.
- Rayner, N., and Coauthors, 2006: Improved analyses of changes and uncertainties in sea surface temperature measured in situ since the mid-nineteenth century: The HadSST2 dataset. *Journal of Climate*, **19**, 446-469.
- Ruff, T., Y. Kushnir, and R. Seager, 2012: Comparing twentieth- and twenty-first-century patterns of interannual precipitation variability over the western United States and northern Mexico. *Journal of Hydrometeorology*, **13**, 366-378.
- Sandeep, S., F. Stordal, P. Sardeshmukh, and G. Compo, 2014: Pacific Walker Circulation variability in coupled and uncoupled climate models. *Climate Dynamics*, **43**, 103-117.
- Santer, B. D., K. E. Taylor, P. J. Gleckler, C. Bonfils, T. P. Barnett, D. W. Pierce, T. M. L. Wigley, C. Mears, F. J. Wentz, W. Bruggemann, N. P. Gillett, S. A. Klein, S. Solomon, P. A. Stott, and M. F. Wehner, 2009: Incorporating model quality information in climate change detection and attribution studies. *Proceedings of the National Academy of Sciences*, **106**, 14778-14783.
- Schubert, S., and Coauthors, 2009: A US CLIVAR project to assess and compare the responses of global climate models to drought-related SST forcing patterns: overview and results. *Journal of Climate*, **22**, 5251-5272.
- Seager, R., N. Naik, and L. Vogel, 2012: Does global warming cause intensified interannual hydroclimate variability? *Journal of Climate*, **25**, 3355-3372.
- Seidel, D., Q. Fu, W. Randel, and T. Reichler, 2008: Widening of the tropical belt in a changing climate. *Nature Geoscience*, **1**, 21-24.
- Smith, T., R. Reynolds, T. Peterson, and J. Lawrimore, 2008: Improvements to NOAA's historical merged land-ocean surface temperature analysis (1880-2006). *Journal of Climate*, **21**, 2283-2296.
- Solomon, A., and M. Newman, 2012: Reconciling disparate twentieth-century Indo-Pacific ocean temperature trends in the instrumental record. *Nature Climate Change*, **2**, 691-699.
- Sperber, K., and D. Kim, 2012: Simplified metrics for the identification of the Madden-Julian oscillation in models. *Atmospheric Science Letters*, **13**, 187-193.
- Sperber, K., S. Gualdi, S. Legutke, and G. V., 2005: The Madden-Julian oscillation in ECHAM4 coupled and uncoupled general circulation models. *Climate Dynamics*, **25**, 117-140.
- Stevenson, S., 2012: Significant changes to ENSO strength and impacts in the twenty-first century: Results from CMIP5. *Geophysical Research Letters*, **39**.
- Stevenson, S., B. Fox-Kemper, M. Jochum, R. Neale, C. Deser, and G. Meehl, 2012: Will there be a significant change to El Nino in the twenty-first century? *Journal of Climate*, **25**, 2129-2145.
- Taylor, K., R. Stouffer, and G. Meehl, 2012: An overview of CMIP5 and the experiment design. *Bulletin of the American Meteorological Society*, **93**, 485-498.
- Tokunaga, H., S. Xie, C. Deser, Y. Kosaka, and Y. Okumura, 2012: Slowdown of the Walker circulation driven by tropical Indo-Pacific warming. *Nature*, **491**, 439-+.
- Trenberth, K., J. Fasullo, and L. Smith, 2005: Trends and variability in column-integrated atmospheric water vapor. *Climate Dynamics*, **24**, 741-758.
- Vecchi, G., and A. Wittenberg, 2010: El Nino and our future climate: where do we stand? *Wiley Interdisciplinary Reviews-Climate Change*, **1**, 260-270.
- Vecchi, G., B. Soden, A. Wittenberg, I. Held, A. Leetmaa, and M. Harrison, 2006: Weakening of tropical Pacific atmospheric circulation due to anthropogenic forcing. *Nature*, **441**, 73-76.
- Watanabe, M., Y. Kamae, and M. Kimoto, 2014: Robust increase of the equatorial Pacific rainfall and its variability in a warmed climate. *Geophysical Research Letters*, **41**, 3227-3232.
- Wittenberg, A., 2015: Low-frequency variations of ENSO. *U.S. Clivar Variations*, 26-31.
- Xie, S., C. Deser, G. Vecchi, J. Ma, H. Teng, and A. Wittenberg, 2010: Global Warming Pattern Formation: Sea Surface Temperature and Rainfall. *Journal of Climate*, **23**, 966-986.
- Yeh, S., J. Kug, B. Dewitte, M. Kwon, B. Kirtman, and F. Jin, 2009: El Nino in a changing climate. *Nature*, **461**, 511-U570.
- Zhou, Z., S. Xie, X. Zheng, Q. Liu, and H. Wang, 2014: Global Warming-Induced Changes in El Nino Teleconnections over the North Pacific and North America. *Journal of Climate*, **27**, 9050-9064.

Figure Captions

Figure 1 Leading EOFs ($^{\circ}\text{C}$) of observed monthly-mean SST anomalies calculated with the ERSSTv3b dataset and associated PCs. PCs for HadISST SST data are also shown. **a)** ENSO-like (cENSO) mode calculated using SST residuals (SSTRs), after removal of the global-mean SST anomalies; **b)** associated cENSO-PC; **c)** cENSO-based composite analysis of time-longitude section of SST anomalies ($^{\circ}\text{C}$) showing the development and decay of El Niño events (5°N - 5°S mean). The temporal information of this composite analysis is derived from the cENSO-PC₁ time series; the spatial information is derived from the cENSO pattern. **d)** Leading mode of SST anomalies after regressing out the cENSO pattern; **e)** associated PC. The PCs are scaled to have zero mean and unit variance. The spatial patterns are scaled to have $^{\circ}\text{C}$ unit amplitude. For each EOF, the total explained space-time variance of the SSTRs is given (in %), along with the spatial average of the eigenvector. Compared to the “global-mean included” case (Figs. S1a-b), the leading modes capturing cENSO and large-scale warming are more clearly separated, and PCs are less sensitive to structural differences between the HADISST1.1 and ERSSTv3b datasets (as expressed by r correlation values).

Figure 2: Observed and simulated hydrological teleconnections driven by temporal variability in the ENSO-like pattern. **a)** cENSO PC and most highly-correlated PC time series for W (PC₁), P (PC₁) and PDSI (PC₂, 3-month lag). Because of the cENSO-PDSI lag, the PDSI time-series is time-shifted by 3 months to

facilitate visual comparison of “between variable” covariance relationships. All monthly time-series are lowpass-filtered. **b-d)** Observed DJF cENSO-driven W, P and PDSI teleconnection patterns. Each pattern is calculated over the length of the W, P and PDSI observational record. The pattern correlation between **c-b** (**c-d**) is 0.67 (0.76) over ocean (land). **e-f): DJF** Teleconnection patterns averaged over the TOP20 models for the 1900-1999 and difference between the 2000-2099 and the 1900-1999 periods. Isolines of the teleconnection patterns for the 1900-1999 period displayed in **e** (light blue and grey lines) are reproduced in **f**. Stippled areas indicate pronounced inter-model agreement ($|S/N| > 1.0$, where S (N) represents the model average (the inter-model standard deviation) of the teleconnection maps).

Figure 3: Model **a-b)** Relationship between model skill in simulating the observed cENSO pattern (as measured by the r_{EOF1} metric) and **a** model skill in simulating observed cENSO variability σ_{OBS} ; **b** the observed teleconnection patterns, r_{TEL} (based here on all calendar months); **c)** Relationship between the amplitude of 21st and 20th century cENSO variability (both calculated as the temporal standard deviation of the detrended monthly-mean pseudo-PC time series); **d)** Relationship between the model skill in simulating the observed cENSO pattern and the overall model-simulated cENSO changes in the 21st century. **e)** DJF teleconnection stationarity, measured as the centered spatial correlation between the P teleconnection patterns for the 1900-1999 and 2000-2099 periods. Metrics displayed in **a-b** are the realization-ensemble mean statistic for each model (see

Table S1). Data in **c-e** are displayed for each individual realization. The TOP20 models are represented with solid symbols. The grey shading in **d** represents the two-tailed 95% confidence interval of internal variability, calculated as $\varepsilon \times 1.96$, where ε is the standard error of the sampling distribution of 100-year overlapping unforced trends in the TOP20 control runs (with overlap=10 years). The green shaded area in **a**, **b** and **d** denotes r_{EOF1} values > 0.83 , the cutoff for definition of the TOP20 models, while the yellow shaded area in **b** indicates the 20 models that best reproduce the observed teleconnections (based on the r_{TEL} metric). The orange dotted lines in panel 3a delimit the 20 models that best reproduce the observed $\sigma_{1979-2012}$, as shown in Fig. 5b of the Supplementary Online Material (SOM).

Figure 4: Decomposition of the total DJF precipitation response (mm/day) to future cENSO events using the TOP20 models. **a)** future (2000-2099) and **b)** present-day (1900-1999) P anomalies (both relative to the same historical baseline) in response to La Niña- and El Niño-like events (based on the CA #1 technique—see text). The respective spatial correlations with the GPCP-based composite maps (computed over the 1979-2012 period) are indicated in the left corner of the panels. **c)** Change in mean DJF P (this panel is independent of the ENSO phase). Note, rectangles mark areas for further regional analysis—see Figure 7. **d)** Enhanced future P response to La Niña- and El Niño-like events from Composite Analysis #2—see text. This amplification component is the difference between future and the present-day *detrended* P composites. Vertical strips

highlight regions with statistically significant differences under a two-sided t-test at a 10% level, with a sample size of 20 models.

Figure 5: Amplification components, as in Fig. 4d, calculated from model subsets projecting an increasing, unchanged, and decreasing amplitude (respectively) of SST cENSO variability. Vertical strips highlight regions with statistically significant differences under a two-sided t-test at a 10% level, with a sample size of 5/10/5 models, respectively.

Figure 6: DJF precipitation **a-b)** along the Equator (2°S - 2°N); and **c-d)** North American Pacific west coast (39°N - 45°N), during El Niño and La Niña events. Results are computed for the TOP20 models, and for the three sets of models classified by the magnitude of temporal variability of the cENSO pseudo-PC (σ). The zonal means are computed from the precipitation composites used to create Fig. 4d and Fig. 5, i.e. based on detrended cENSO and P fields. The multi-model average of σ over 1900-1999 is 1.07 (0.96) when calculated using the 5 (5) models projecting a decrease (increase) in SST cENSO magnitude, and 0.93 when computed using the models with no discernible change in σ .

Figure 7: Regionally-averaged historical and future P anomalies in response to cENSO events in the seven regions indicated by the rectangles in Fig. 4c. The future cENSO-driven P anomalies can be decomposed into a change in the P mean-state (dashed lines, calculated from Fig. 4c), the historical cENSO-driven P

response (the light blue and red boxes, calculated from Fig. 4b), and the amplification of this historical P response (the dark blue and red boxes, calculated from Fig. 4d) (also expressed in % of the historical response). The whiskers represent the model uncertainties in changes in the amplitude of cENSO-driven SST variability (from Fig. 5).

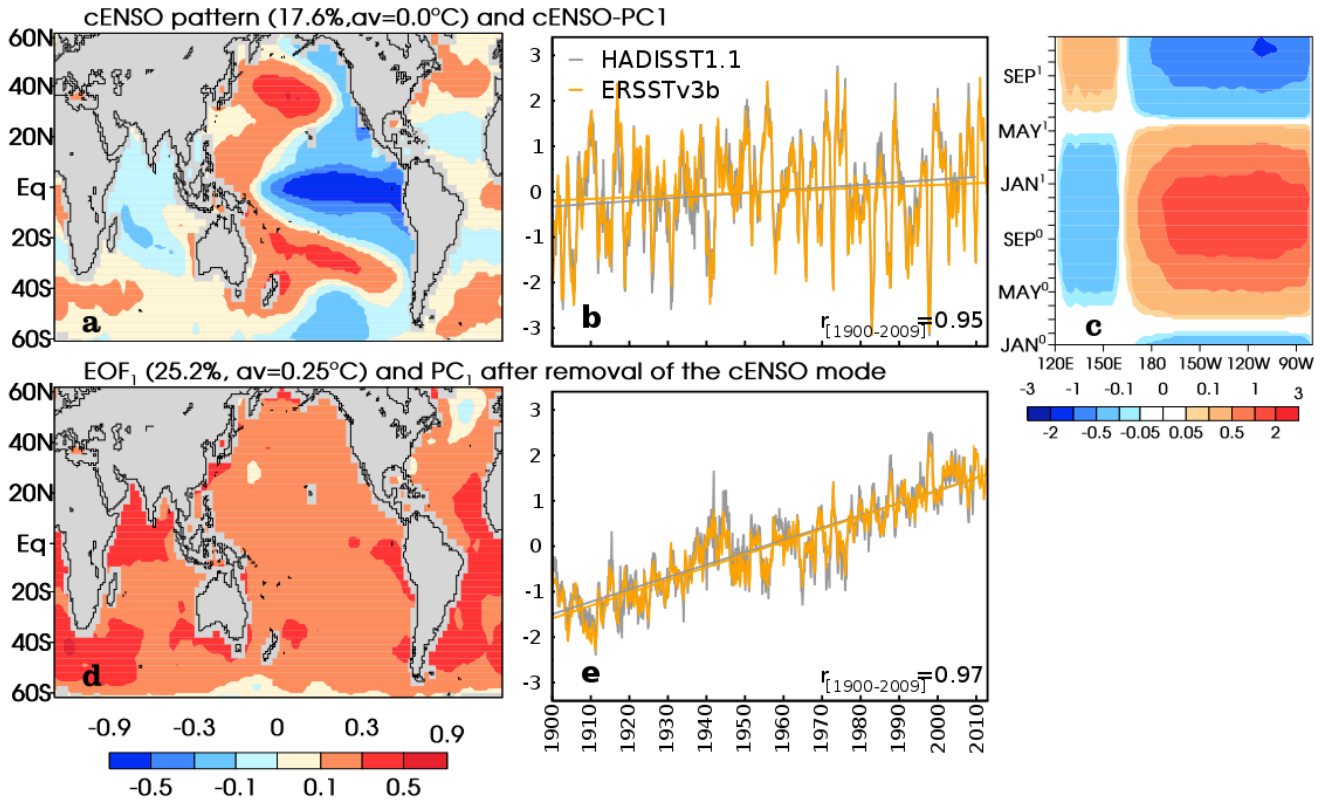
Figure 1

Figure 1 Leading EOFs (°C) of observed monthly-mean SST anomalies calculated with the ERSSTv3b dataset and associated PCs. PCs for HadISST SST data are also shown. **a)** ENSO-like (cENSO) mode calculated using SST residuals (SSTRs), after removal of the global-mean SST anomalies; **b)** associated cENSO-PC; **c)** cENSO-based composite analysis of time-longitude section of SST anomalies (°C) showing the development and decay of El Niño events (5°N-5°S mean). The temporal information of this composite analysis is derived from the cENSO-PC₁ time series; the spatial information is derived from the cENSO pattern. **d)** Leading mode of SST anomalies after regressing out the cENSO pattern; **e)** associated PC. The PCs are scaled to have zero mean and unit variance. The spatial patterns are scaled to have °C unit amplitude. For each EOF, the total explained space-time variance of the SSTRs is given (in %), along with the spatial average of the eigenvector. Compared to the “global-mean included” case (Figs. S1a-b), the leading modes capturing cENSO and large-scale warming are more clearly separated, and PCs are less sensitive to structural differences between the HADISST1.1 and ERSSTv3b datasets (as expressed by r correlation values).

Figure 2

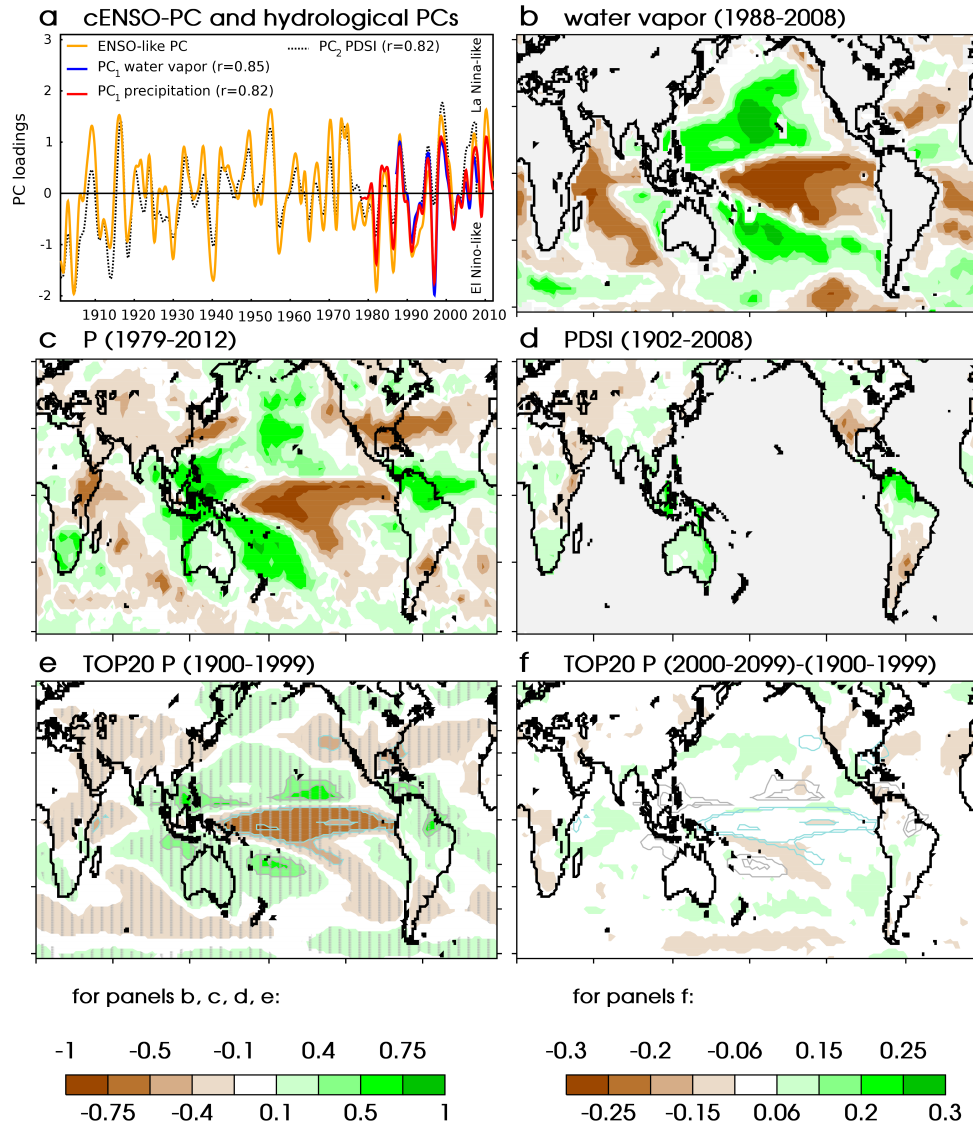


Figure 2: Observed and simulated hydrological teleconnections driven by temporal variability in the ENSO-like pattern. **a)** cENSO PC and most highly-correlated PC time series for W (PC₁), P (PC₁) and PDSI (PC₂, 3-month lag). Because of the cENSO-PDSI lag, the PDSI time-series is time-shifted by 3 months to facilitate visual comparison of “between variable” covariance relationships. All monthly time-series are lowpass-filtered. **b-d)** Observed DJF cENSO-driven W, P and PDSI teleconnection patterns. Each pattern is calculated over the length of the W, P and PDSI observational record. The pattern correlation between **c-b** (**c-d**) is 0.67 (0.76) over ocean (land). **e-f):** DJF Teleconnection patterns averaged over the TOP20 models for the 1900-1999 and difference between the 2000-2099 and the 1900-1999 periods. Isolines of the teleconnection patterns for the 1900-1999 period displayed in **e** (light blue and grey lines) are reproduced in **f**. Stippled areas indicate pronounced inter-model agreement ($|S/N| > 1.0$, where S (N) represents

the model average (the inter-model standard deviation) of the teleconnection maps).

Figure 3

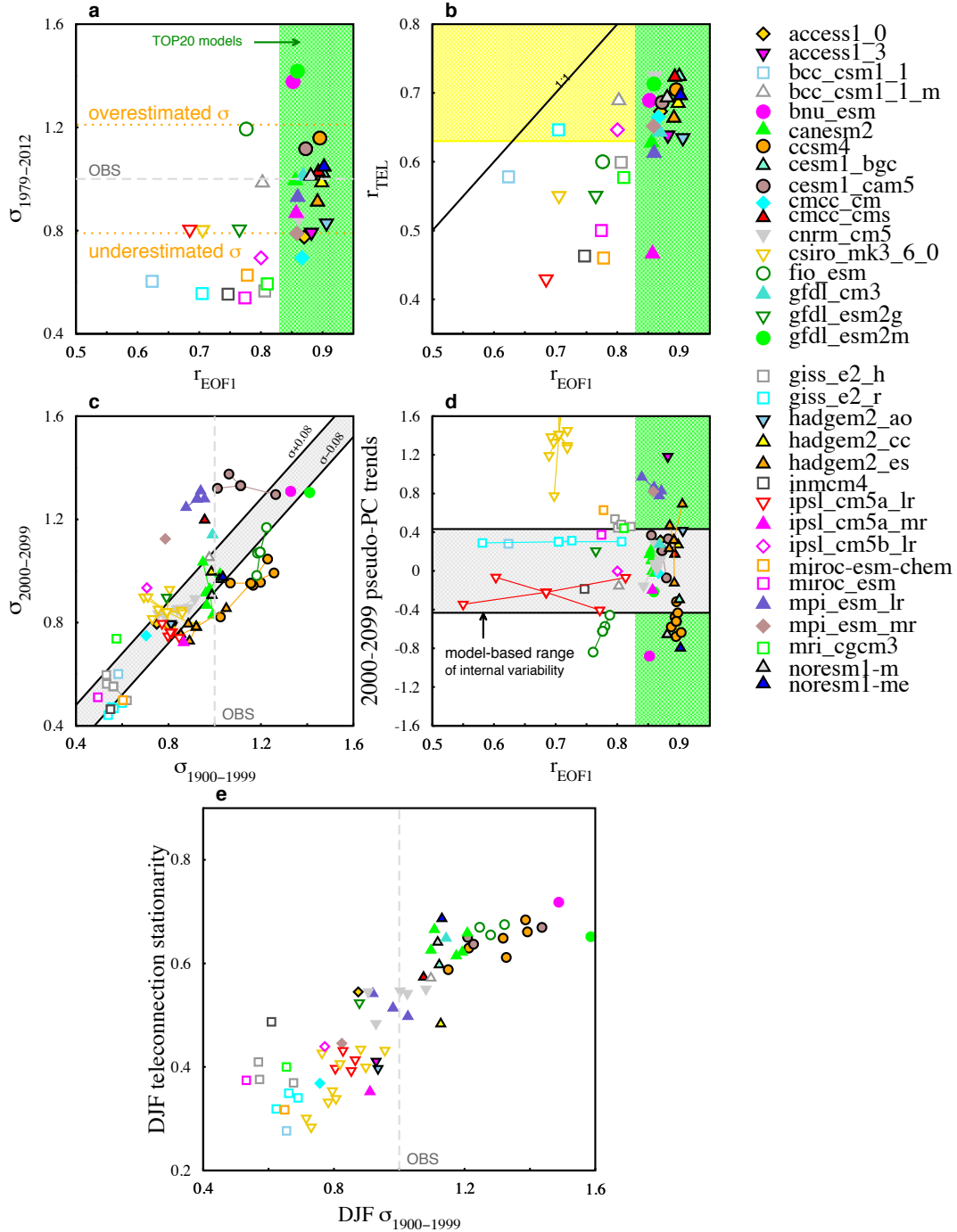


Figure 3: Model **a-b)** Relationship between model skill in simulating the observed cENSO pattern (as measured by the r_{EOF1} metric) and **a** model skill in simulating observed cENSO variability σ_{OBS} ; **b** the observed teleconnection patterns, r_{TEL} (based here on all calendar months); **c)** Relationship between the amplitude of 21st and 20th century cENSO variability (both calculated as the temporal standard deviation of the detrended monthly-mean pseudo-PC time series); **d)** Relationship between the

model skill in simulating the observed cENSO pattern and the overall model-simulated cENSO changes in the 21st century. **e)** DJF teleconnection stationarity, measured as the centered spatial correlation between the P teleconnection patterns for the 1900-1999 and 2000-2099 periods. Metrics displayed in **a-b** are the realization-ensemble mean statistic for each model (see Table S1). Data in **c-e** are displayed for each individual realization. The TOP20 models are represented with solid symbols. The grey shading in **d** represents the two-tailed 95% confidence interval of internal variability, calculated as $\varepsilon \times 1.96$, where ε is the standard error of the sampling distribution of 100-year overlapping unforced trends in the TOP20 control runs (with overlap=10 years). The green shaded area in **a**, **b** and **d** denotes r_{EOF1} values > 0.83 , the cutoff for definition of the TOP20 models, while the yellow shaded area in **b** indicates the 20 models that best reproduce the observed teleconnections (based on the r_{TEL} metric). The orange dotted lines in panel 3a delimit the 20 models that best reproduce the observed $\sigma_{1979-2012}$, as shown in Fig. 5b of the Supplementary Online Material (SOM).

Figure 4

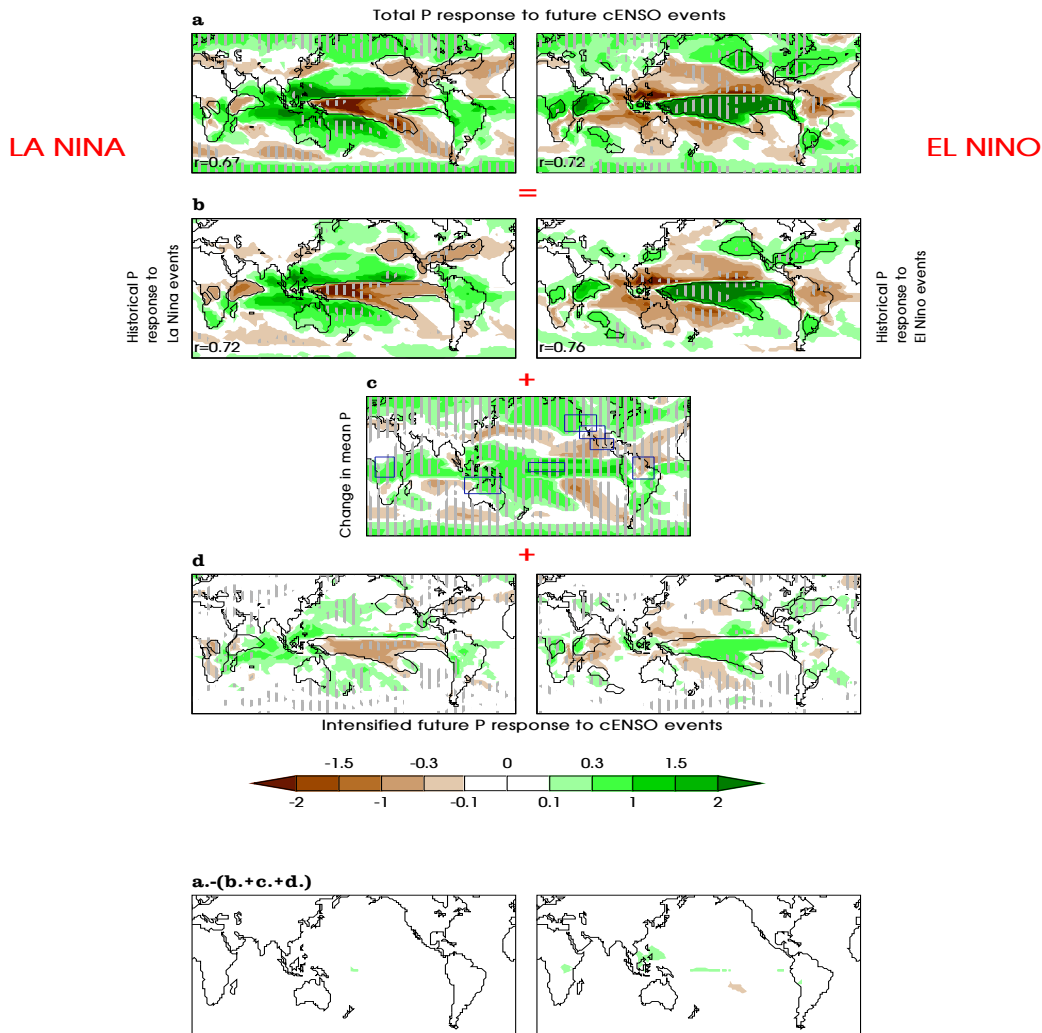


Figure 4: Decomposition of the total DJF precipitation response (mm/day) to future cENSO events using the TOP20 models. **a)** future (2000-2099) and **b)** present-day (1900-1999) P anomalies (both relative to the same historical baseline) in response to La Niña- and El Niño-like events (based on the CA #1 technique—see text). The respective spatial correlations with the GPCP-based composite maps (computed over the 1979-2012 period) are indicated in the left corner of the panels. **c)** Change in mean DJF P (this panel is independent of the ENSO phase). Note, rectangles mark areas for further regional analysis—see Figure 7. **d)** Enhanced future P response to La Niña- and El Niño-like events from Composite Analysis #2—see text. This amplification component is the difference between future and the present-day *detrended* P composites. Vertical strips highlight regions with statistically significant differences under a two-sided t-test at a 10% level, with a sample size of 20 models.

Figure 5

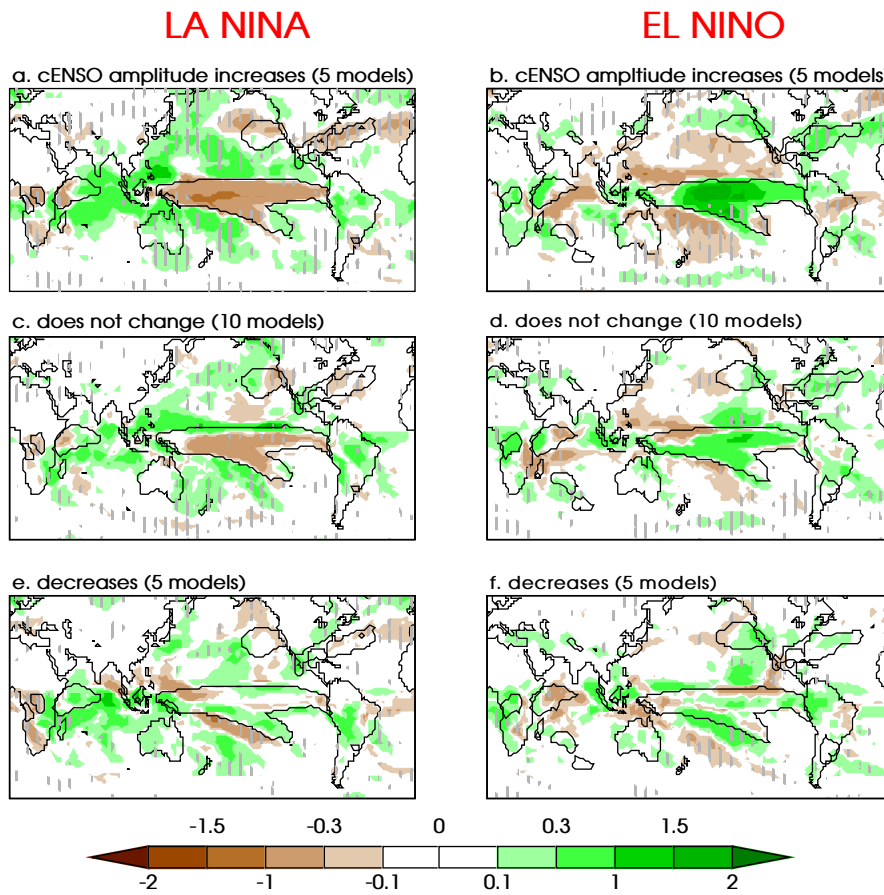


Figure 5: Amplification components, as in Fig. 4d, calculated from model subsets projecting an increasing, unchanged, and decreasing amplitude (respectively) of SST cENSO variability. Vertical strips highlight regions with statistically significant differences under a two-sided t-test at a 10% level, with a sample size of 5/10/5 models, respectively.

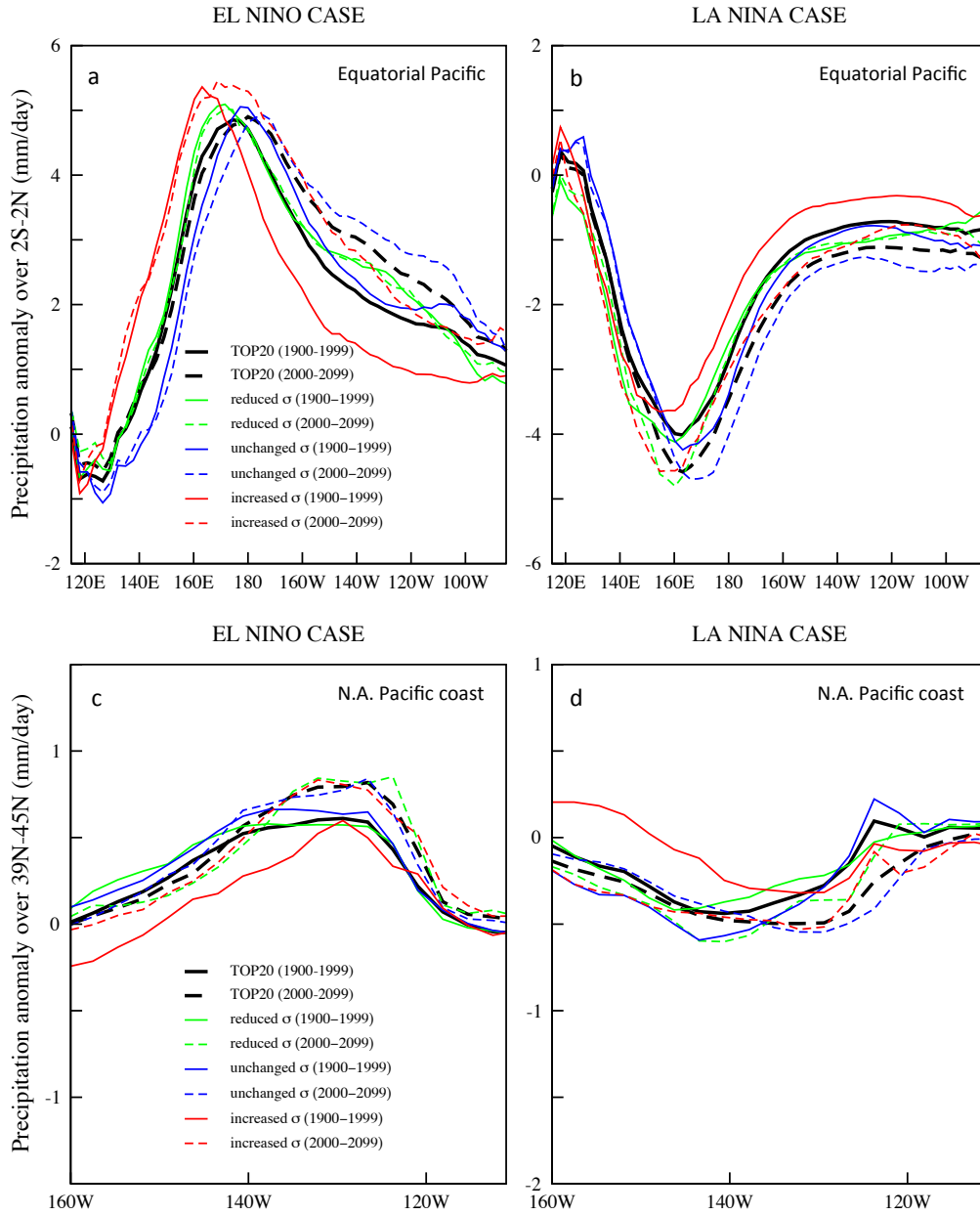
Figure 6

Figure 6: DJF precipitation **a-b)** along the Equator (2°S-2°N); and **c-d)** North American Pacific west coast (39°N-45°N), during El Niño and La Niña events. Results are computed for the TOP20 models, and for the three sets of models classified by the magnitude of temporal variability of the cENSO pseudo-PC (σ). The zonal means are computed from the precipitation composites used to create Fig. 4d and Fig. 5, i.e. based on detrended cENSO and P fields. The multi-model average of σ over 1900-1999 is 1.07 (0.96) when calculated using the 5 (5) models projecting a decrease (increase) in SST cENSO magnitude, and 0.93 when computed using the models with no discernible change in σ .

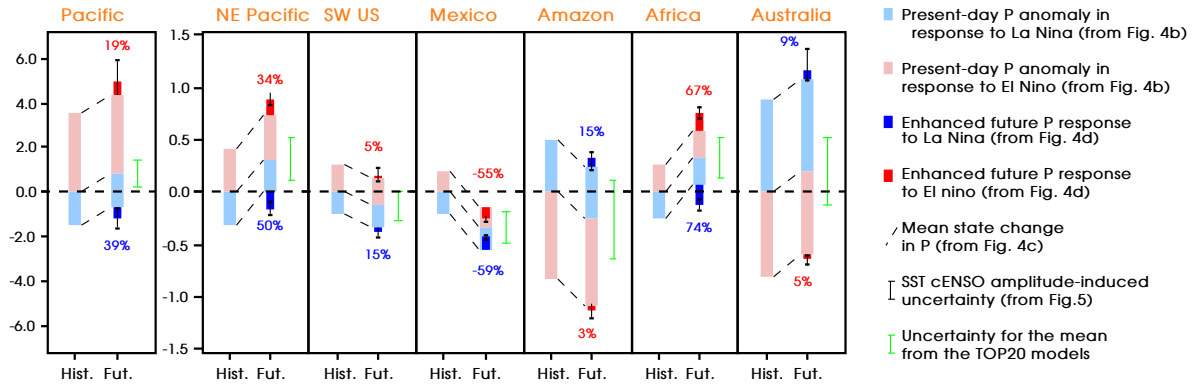
Figure 7

Figure 7: Regionally-averaged historical and future P anomalies in response to cENSO events in the seven regions indicated by the rectangles in Fig. 4c. The future cENSO-driven P anomalies can be decomposed into a change in the P mean-state (dashed lines, calculated from Fig. 4c), the historical cENSO-driven P response (the light blue and red boxes, calculated from Fig. 4b), and the amplification of this historical P response (the dark blue and red boxes, calculated from Fig. 4d) (also expressed in % of the historical response). The whiskers represent the model uncertainties in changes in the amplitude of cENSO-driven SST variability (from Fig. 5).